Powder Technology xxx (xxxx) xxx

Contents lists available at ScienceDirect

Powder Technology

journal homepage: www.elsevier.com/locate/powtec

Visco-elastic sintering kinetics in virgin and aged polymer powders

J.E. Alvarez [a,*], H. Snijder [b], T. Vaneker [b], H. Cheng [a,c], A.R. Thornton [a], S. Luding [a], T. Weinhart [a]

[a] Multi-scale Mechanics, Faculty of Engineering Technology, MESA+, University of Twente, Drienerlolaan 5, 7522 NB, Enschede, The Netherlands
[b] Department of Design, Production and Management, Faculty of Engineering Technology, University of Twente, Drienerlolaan 5, 7522 NB, Enschede, The Netherlands
[c] Department of Civil Engineering, Faculty of Engineering Technology, University of Twente, Drienerlolaan 5, 7522 NB, Enschede, The Netherlands

ARTICLE INFO

Article history:
Received 22 September 2021
Received in revised form 19 November 2021
Accepted 20 November 2021
Available online xxxx

Keywords:
Polymer powders
Sintering
Visco-elastic kinetics
Discrete element method
Bayesian calibration

ABSTRACT

This work provides a novel discrete element method (DEM) framework for modelling the visco-elastic sintering kinetics in virgin and aged polymer powders. The coalescence of particle pairs, over long times, is described by a combined three-stage model of the sintering process, where each stage is dominated by a different driving force: adhesive contact force, adhesive inter-surface force and surface tension. The proposed framework is implemented in MercuryDPM, an open-source package for discrete particle simulations. To quantitatively calibrate the particle-scale parameters, Bayesian filtering is used. Experimental data on Polystyrene (PS), Polyamide 12 (PA12), and PEEK powders, both virgin and aged, are analysed and confirm over a wide range of times the existence of the three distinct sintering mechanisms. In good agreement with the experimental observations, the estimation of sintering time is achieved with a significant accuracy compared to Frenkel's model. This study provides an efficient and reliable approach for future studies of strength evolution in powder-bed fusion processes.

1. Introduction

Selective laser sintering is a modern technique to build 3D objects from visco-elastic powders. In the process, a laser beam heats selected particles resulting in solid sinter-necks at the contact points. It leads to a solidified surface layer, which is augmented with new powder deposition and their respective sintering. If the cohesion between particles is weak, texture defects arise on the sintered object such as delamination, distortion and dimensional inaccuracies [1,2]. Furthermore, external effects from powder spattering and laser socking may induce additional forces along the cohesion. Therefore, an appropriate sintering time needs to be set to ensure sufficient cohesion among the particles. This sintering time depends on the powder properties and the specifications of the laser beam.

To predict sintering, Frenkel's model is commonly employed [3]. This model describes the rate of sintering between adjacent particles by equating the rate of work done by surface tension to the rate of energy dissipation due to viscous flow. It results in a power law, which reproduces the neck-growth kinetics at constant time. However, predictions based on Frenkel's model disagree with experimental observations in the early stage of visco-elastic sintering [4–7]. The reason is that a single power law does not account for the non-linear behaviour in visco-elastic powders. To overcome this fact, Lin et al. [8] introduced a time-dependent neck growth model that depends on three sintering mechanisms. First, the neck radius is determined using a global energy balance, equating the work of adhesion to the change of potential energy [9]. Second, the neck growth is driven by adhesive inter-surface forces, accommodated by visco-elastic deformations. Third, the sintering mechanism proposed by Frenkel drives the sintering forward.

Different approaches to predict contact interaction are found in the literature, either using Frenkel's model or visco-elastic adhesive contact models [10–17]. Nonetheless, the micro-mechanical calibration remains a tremendous challenge [15,18], mainly due to the diversity of particle surfaces, shapes, disorder and anisotropy. Furthermore, rheological flow properties are difficult to obtain when visco-elastic powders are recycled from a previous sintering process, for instance.

This work introduces a novel time-dependent sintering DEM approach to estimate the visco-elastic coalescence of polymer particles at short and long times. The approach relies on the three-stage sintering scheme proposed by Lin et al. [8]. First, the sintering model is integrated into the visco-elastoplastic and dissipative contact model proposed by Luding [19], using the rate of plastic overlap. Then, particle pair interactions are computed utilizing MercuryDPM [20]. The calibration of the micro-mechanical parameters is performed by the Bayesian calibration

* Corresponding author.
E-mail addresses: j.e.alvareznaranjo@utwente.nl (J.E. Alvarez), h.cheng@utwente.nl (H. Cheng), t.weinhart@utwente.nl (T. Weinhart).

https://doi.org/10.1016/j.powtec.2021.11.044

tool developed by Cheng et al. [21]. The current approach uses experimental data from PA12 in both virgin and aged states, PS as studied by Hejmady et al. [22], and PEEK as presented by Beretta et al. [6].

2. Sintering model for polymer powders

When a thermal field is defined on two contacting visco-elastic particles, adhesive and surface-tension forces act to sinter the two into a single particle. According to Lin et al. [8], the visco-elastic kinetics during the sintering process may be described within three different stages, each dominated by a different sintering mechanism: contacts formation due to elastic and adhesive forces; contact growth driven by adhesive inter-surface forces, accommodated by visco-elastic deformation; and contact growth driven by surface tension, accommodated by viscous flow. These three mechanisms are bound by the interplay between time and length scales set by intrinsic polymer properties, including compliance properties and visco-elastic interactions during the growth phase. A regime map for the three different stages is illustrated in Fig. 1, similar to that developed by Lin et al. [8].

In the first stage, the sintering kinetics is described by balancing the work exerted by adhesive forces within the contact area between the particles and the work of the visco-elastic deformation. Johnson, Kendall, and Roberts (JKR [9]) expressed that under zero applied load, the contact between two particles exhibits an initial flattened contact radius a_0. Thereby, with zero applied load, the two contacting particles approach an equilibrium state in which the elastic repulsion is balanced by the adhesive attraction of the particles. JKR analysis assumes that the particles are linearly elastic, and the strain theory is used since the contact area is smaller than the radius of the particles. The schematic illustration of this first stage is presented in Fig. 2.

The non-dimensional neck radius a_0/R was derived by JKR at very short times ($t < t_0$) for the equilibrium deformation of two elastic bodies under the influence of surface tension. Thus, the elastic repulsion using the Hertz equation is balanced by the adhesive traction of the particles, giving

$$\frac{a_0}{R} = \left(\frac{9\pi(1-\nu^2)\gamma}{\mathrm{ER}}\right)^{1/3}, \tag{1}$$

where γ is the surface tension [Nm^{-1}], ν is Poisson's ratio, E is Young's modulus [Pa]. Within this adhesive stage, the contact radius is not time-dependent due to the time-invariant modulus, which is that of a glassy solid, and a very rapid swing-in period, which is neglected.

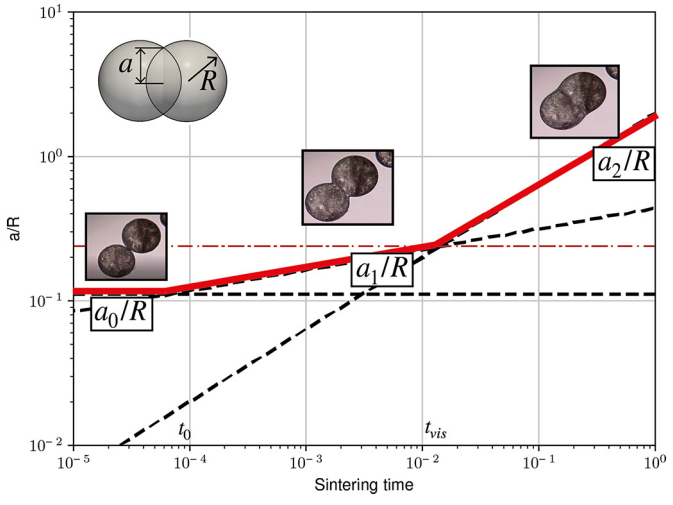

Fig. 1. Log-log plot of the three-stage model for the growth of the dimensionless contact radius a/R with time. If $t < t_0$, a_0/R is a constant derived from JKR theory. For intermediate times $t_0 < t < t_{vis}$, a power-law behaviour emerges, $a_1/R \sim t^{1/7}$, exhibiting only weakly time-dependent growth. For $t > t_{vis}$, $a_2/R \sim t^{1/2}$, indicative of viscous sintering, which results in faster growth.

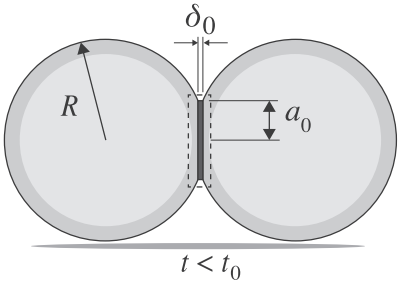

Fig. 2. Schematic of contact area following the JKR model. An instantaneous flattened contact of radius a_0, corresponding to sphere-interpenetration δ_0, is formed to ensure an equilibrium state of two contacting particles without external forces.

After the initial contact ($t > t_0$, see Fig. 1), the second stage of neck growth is due to visco-elastic deformation of the particles balanced by inter-surface adhesive forces acting in the region around the contact area, as illustrated in Fig. 3.

In this stage, polymers can exhibit all intermediate-range of properties between an elastic solid and a viscous liquid. For this, two main phenomena required being involved while the visco-elastic particles are bonding: creep compliance and stress relaxation. First, creep $C(t)$ [Pa^{-1}] quantifies the capacity of a material to flow in response to a sudden applied stress. Second, stress relaxation indicates the moment at which a visco-elastic material relieves stress under strain. Therefore, the strain rate is a function of time under instantaneous application of constant stress σ, expressed in a non-Hookean fashion as

$$\varepsilon(t) = C(t)\sigma. \tag{2}$$

The contact creep compliance is a useful metric that quantifies a unique mechanical response, defined by

$$C(t) = C_0 + C_1 t^m, \tag{3}$$

where $C_0 = (1-\nu^2)/E$ represents the instantaneous compliance [Pa^{-1}], C_1 [$\mathrm{Pa}^{-1}\ \mathrm{s}^{-1}$] is a material property, called "fluidity" in our work, and $0 < m < 1$. To treat the problem of sintering due to adhesive forces, the region around the contact area is modelled as a crack, computing the adhesive traction between the two-particle surfaces using a cohesive traction theory. Theoretically, virtual elements are attached to the particle surfaces in order to mimic the adhesive traction. These elements describe inter-surface adhesive forces in the regime of visco-elastic deformation. By assuming that the virtual element is smaller than the contact radius a, the visco-elastic contact problem can be decomposed into an outer problem of contact mechanics, and an inner problem of local adhesive bonding [8]. The contact radius a approaches to the radius R by the reference contact stress field $\sigma(r,t) \approx \frac{K^R}{\sqrt{2\pi(a-r)}}$, which indicates a singularity at the contact edge. The strength of the singularity K^R is related to the contact radius and the external loading history, which depends on the rate at which strain increases for constant applied stress (creep compliance). The Dugdale-Barenblatt cohesive zone model is used to represent the intersurface adhesive forces, assuming that adhesive force σ is constant inside the cohesive zone as long as the separation distance is less than the critical separation distance δ_c [m]. The separation distance is specified to ensure the work of adhesion, defined as the range of the adhesive force. Then, the work of adhesion is computed as $W = \sigma\delta_c$. The prediction of the rate of bonding $\dot{a}$ is coupled with the strength of the singularity at the tip by Lin et al. [8], which results

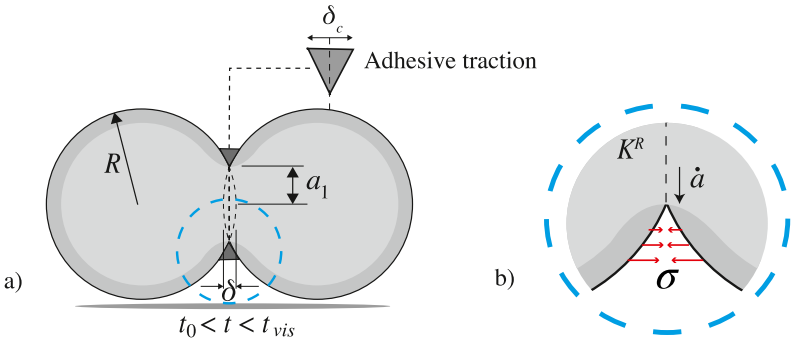

Fig. 3. (a) Schematic of visco-elastic contact growth for $t_0 < t < t_{visc}$ driven by adhesive traction. Forces act normal to the contact plane. (b) Inner problem of local adhesive bonding.

$$\dot{a} = \frac{\pi\gamma}{2c_m^2 C_0 \sigma^2}\left(\frac{C_1\gamma_m}{C_0 c_m}\right), \tag{4}$$

where $c_m = (2m+1)/(m+1)$, and $\gamma_m = (4/\pi)^{1/2}\Gamma(m+1)\Gamma(m+1.5)$, with Γ as the gamma function of adhesion. By solving the evolution of the contact radius in Eq. (4), the estimation of a is obtained as function of the creep response of the material

$$a = a_0^{\frac{3(m+1)}{4m+3}}\left(\frac{4m+3}{m}\frac{\pi\gamma}{2c_m^2 C_0\sigma^2}\left(\frac{C_1\gamma_m}{C_0 c_m}\right)\right)^{\frac{m}{4m+3}} t^{\frac{m}{4m+3}}, \tag{5}$$

where the first term of the Eq. (5) indicates the formation of an initial elastic JKR contact (Eq. (1)), and a visco-elastic transition followed by creeping contact growth for times $t > (C_0/C_m)^{1/m}$. It leads to the exact long time solution for visco-elastic contact growth driven by adhesive traction with a power-law of $t^{m/(4m+3)}$, derived by Hui et al. [8]. Thus, the growth of the contact radius can be computed by

$$\frac{a}{R} = \left(\frac{9\pi}{2}\right)^{\frac{m+1}{4m+3}}\left[\frac{4m+3}{m}\frac{\pi}{4c_m^2}\left(\frac{\delta_c}{R}\right)^2\right]^{\frac{m}{4m+3}}\left(\frac{\gamma_m}{c_m}\frac{2C_1\gamma}{R}\right)^{\frac{1}{4m+3}} t^{\frac{m}{4m+3}}. \tag{6}$$

For intermediate times in the interval $t_0 < t < t_{vis}$, the growth of contact radius a_1 is predicted to be $t^{1/7}$ for a Maxwell material, where $m = 1$. This results in

$$\frac{a_1}{R} = \left(\frac{63\pi^3}{16}\right)^{1/7}\left(\frac{\delta_c}{R}\right)^{2/7}\left(\frac{2C_1\gamma t}{R}\right)^{1/7}. \tag{7}$$

Subsequently, the sintering problem is treated in the third stage for long times ($t > t_0$). It assumes that the visco-elastic particles achieve stress relaxation due to molecular rearrangement, and the extent of recovery is directly proportional to the formerly applied stress. The neck growth kinetics is related to the action of surface tension in the viscous flow regime (see Fig. 1). The schematic representation is shown in Fig. 4.

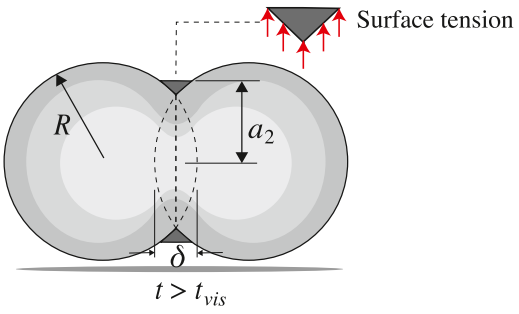

Fig. 4. Schematic of contact growth driven by surface tension and accommodated by viscous flow. Forces act perpendicular to the contact plane.

The growth of the contact radius a_2 was initially derived by Frenkel [3], showing that for a Newtonian fluid, the evolution of a_2 may fulfil a scaling law, which is expected to be well-approximated by the last part of Eq. (5), where is equated the rate of surface tension work to the viscous flow energy dissipation rate, giving

$$\frac{a_2}{R} = \left(\frac{8C_1\gamma t}{R}\right)^{1/2}. \tag{8}$$

By defining a as the maximum of the three different models, $a = \max(a_0, a_1, a_2)$, it is possible to include each stage of the sintering process into a DEM approach. In the following chapter, we discuss how to incorporate the neck growth models (Eq. (1), Eq. (7), Eq. (8)) into the visco-elastoplastic contact model proposed by Luding [19].

3. DEM for visco-elastic sintering

To describe the sintering of discrete particles, DEM is highly suitable. Particles are assumed to be rigid and interact via contact forces. The computation of the forces, acting between particle pairs, are determined using contact models. In this work, we apply the visco-elastoplastic and dissipative model proposed by Luding [19], using MercuryDPM [20] to compute particle pair interactions. Fig. 5 illustrates the contact model.

The elastoplastic and dissipative model computes the repulsive elastoplastic forces during compression (loading) between the particles using a loading stiffness k_1. The unloading process follows the slope of $\hat{k}_2$, which varies between k_1 and k_2, depending on the plastic deformation at zero force δ_{ij}^0. To track the plastic deformation, the maximum plastic overlap δ_{ij}^{max} is stored, and used to compute the zero-force overlap as

$$\delta_{ij}^0 = \frac{\hat{k}_2 - k_1}{\hat{k}_2}\delta_{ij}^{max}. \tag{9}$$

The minimum force overlap δ_{ij}^{min} is computed as

$$\delta_{ij}^{min} = \frac{\hat{k}_2}{\hat{k}_2 + k_c}\delta_{ij}^0. \tag{10}$$

Thereby, the overlap δ_{ij} defines the deformation measurement as

$$\delta_{ij} = (R_i + R_j) - (\mathbf{r}_i - \mathbf{r}_j)\cdot\mathbf{n}, \tag{11}$$

where $\mathbf{r}_i$ and $\mathbf{r}_j$ are the particle positions with unit vector $\mathbf{n} = (\mathbf{r}_i - \mathbf{r}_j)/|\mathbf{r}_i - \mathbf{r}_j|$, and R_i and R_j are the particle radii. If the unloading stiffness $\hat{k}_2$ becomes equal to k_2, the force remains on the corresponding limit elastoplastic branch with the same slope.[1] For overlaps smaller than

[1] It avoids unrealistic large overlaps, also approximating the melt incompressibility with rather low stiffness, in order to have the computation time-step not too small.

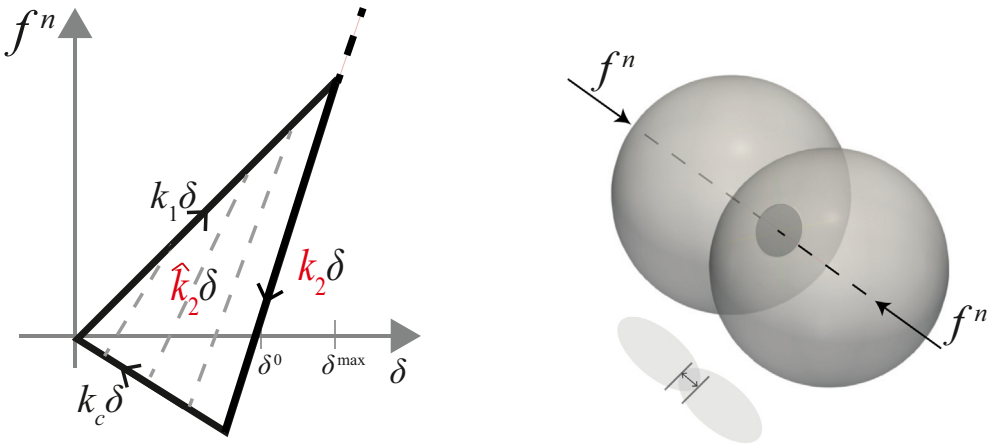

Fig. 5. (Left) Visco-elastoplastic contact law. The contact displacement is related to δ (overlap) and the normal contact force f^n. Right/left-pointing arrows are used to distinguish the forces obtained during the loading and unloading stages, respectively. (Right) Two particle contact with overlap δ.

δ_{ij}^{max}, the unloading stiffness is interpolated linearly between k_2 and k_1 as

$$\hat{k}_2 = \left\{ \begin{array}{lll} k_1 + (k_2 - k_1)\dfrac{\delta_{ij}^{max}}{\varphi_f R_{ij}} & \text{if} & \delta_{ij} < \delta_{ij}^{max} \\ k_2 & \text{if} & \delta_{ij} \geq \delta_{ij}^{max} \end{array} \right\}, \tag{12}$$

where φ_f is the dimensionless plasticity depth, set such that fully merged particles have a contact radius $a/R = \sqrt[3]{2}$. R represents the harmonic mean of the particle radii, $R = 2R_1R_2/(R_1 + R_2)$. After the contact force becomes negative, for $\delta_{ij} < \delta_{ij}^0$, the model introduces cohesive forces using the cohesion stiffness k_c. Thus, the normal force f_{ij}^n between two particles in contact ($\delta_{ij} > 0$) describes the interaction as

$$f_{ij}^n = -f_{ij}^a + \left\{ \begin{array}{lll} k_1\delta_{ij} & \text{if} & \delta_{ij} > \delta_{ij}^{max} \\ \hat{k}_2(\delta_{ij} - \delta_{ij}^0) & \text{if} & \delta_{ij}^{min} < \delta_{ij} \leq \delta_{ij}^{max} \\ -k_c\delta_{ij} & \text{if} & 0 < \delta_{ij} \leq \delta_{ij}^{min} \end{array} \right\} - \gamma^n v_{ij}^n. \tag{13}$$

The adhesive force $f_{ij}^a = k_1\delta_a$ is assumed constant, large enough to reach the equilibrium of the first sintering mechanism, see Eq. (1). For small displacements around some equilibrium state, this hysteretic elastoplastic model does not contain strong dissipation. Therefore, to allow for stronger dissipation and thus faster relaxation, a viscous dissipative force is included in the normal direction. The viscous dissipation coefficient is set to $\gamma^n = \sqrt{2mk_1}/(\sqrt{\pi} + \sqrt{\log e})\log e$, such that we obtain a constant restitution coefficient e. Note, this assumes that e is measured in the elastic regime, i.e. $\delta_{ij} < R$. After the model parameters k_2 and γ are specified, the time-step of the simulation t_{DEM} has to be chosen such that

$$t_{DEM} \approx t_c/50, \tag{14}$$

where t_c represents the collision time on the contact level. For a detailed analytical model treatment, see [19].

3.1. Rate of plastic overlap

To include the sintering behaviour proposed by Lin et al. [8] in the contact description (Eq. (13)), we compute the rate of the plastic overlap $\dot{\delta}_{ij}^0$ using a novel approach. Knowing that the overlap between the particles nearly equals the plastic overlap, $\delta_{ij} \approx \delta_{ij}^0$ for stiff particles ($k_1 > (f_{ij}^n + f_{ij}^a)/R$), the contact radius may be approximated as $a/R \approx \sqrt{\delta_{ij}/R}$ (small overlaps $\delta_{ij}^0 < R$). It can be controlled by setting the growth rate $\dot{\delta}_{ij}^0$ according to Eq. (1), Eq. (7), Eq. (8). First, δ_{ij}^0 is derived below the JKR equilibrium a_0/R, by satisfying $f_{ij}^n = f_{ij}^a$. Second, the computation of $\dot{\delta}_{ij}^0$ is derived within the visco-elastic deformation regime a_1/R, until the neck growth reaches the intersection point at a_{vis}/R,

$$\dot{\delta}_{ij}^0 = \frac{9}{2}\frac{\pi^3\delta_c^2R^{1/2}C_1\gamma}{2^{5/7}\delta_{ij}^{7/2}}\frac{f_{ij}^n}{f_{ij}^a}, \tag{15}$$

where δ_c is the cohesive separation distance, and C_1 is the material fluidity. The calculation of a_{vis}/R is based on the contribution of both JKR and visco-elastic contact during $t_0 < t < t_{vis}$. The explicit expressions for t_0 and t_{vis} can be obtained by plotting Eq. (1), Eq. (7), Eq. (8) and finding the intersection of the curves, see Fig. 1, then

$$t_{vis} = \frac{1}{16}\left(\frac{63\pi^3}{2}\right)^{2/5}\frac{R}{C_1W}\left(\frac{\delta_c}{R}\right)^{4/5}. \tag{16}$$

Substituting Eq. (16) into the expression of the second neck growth (Eq. (7)), gives

$$a_{vis}/R = (63\pi^3)^{1/5}\left(\frac{\delta_c}{8R}\right)^{2/5}. \tag{17}$$

Finally, $\dot{\delta}_{ij}^0$ is derived from Eq. (8) to define sintering at long times, modelled as

$$\dot{\delta}_{ij}^0 = C_1\gamma\frac{f_{ij}^n}{f_{ij}^a}. \tag{18}$$

All parameters of the contact model might vary with temperature, but this is neglected for simplicity assuming constant values. The only adjustable parameters in the simulations are δ_c and C_1. These parameters are calibrated using experimental data as discussed in Section 4. Since friction forces act in the tangential direction, they do not affect the normal forces calculated via this approach, and therefore they are not discussed in this paper. For a detailed explanation, see [23].

4. Methodology

In Section 4.1, the sintering experiments of PA12 powder is described. Then in Section hyperlink4.24.2, we present the coupled implementation MercuryDPM and `GrainLearning` to calibrate the contact model based on the experimental data.

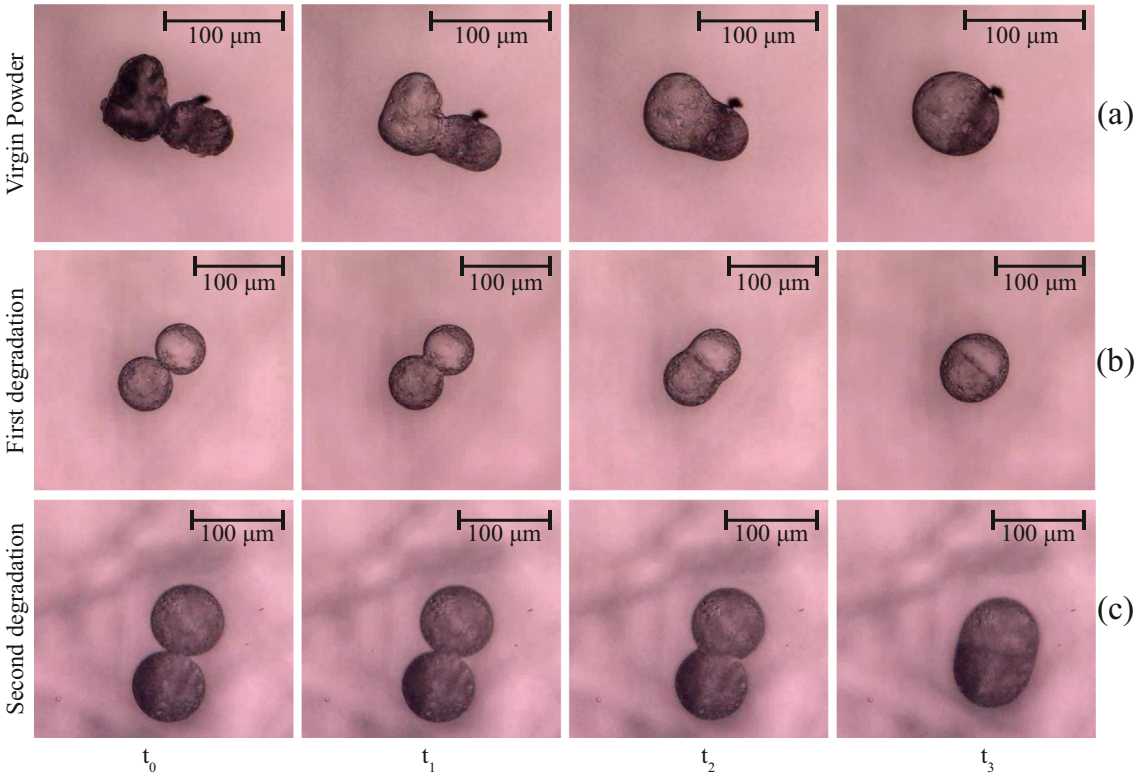

Fig. 6. (a) sintering of virgin particles at $t_0 = 0.0$ s, $t_1 = 2.0$ s, $t_2 = 3.5$ s, $t_3 = 8.5$ s. (b) Sintering of particles in a first heating at $t_0 = 0.0$ s, $t_1 = 2.0$ s, $t_2 = 6.0$ s, $t_3 = 14.0$ s. (c) Sintering of particles in a second heating at $t_0 = 0.0$ s, $t_1 = 2.0$ s, $t_2 = 6.0$ s, $t_3 = 18.0$ s.

4.1. Sintering experiments on PA12 powder

Sintering experiments on PA12 were conducted with PA2200 performance powder for laser sintering supplied by EOS E-Manufacturing solutions. This powder material is a semi-crystalline thermoplastic with a melting point of about 180 °C. The sintering measurements were recorded by a Keyence VHX 5000 digital microscope equipped with a Linkam THMS600 heating stage. It included a glass plate located on the top of the stage with a diameter of 22 mm and thickness of 1.7 mm.

Before starting the experiment, a fine silicon oil was placed on the plate and heated at a temperature of 300 °C to distribute

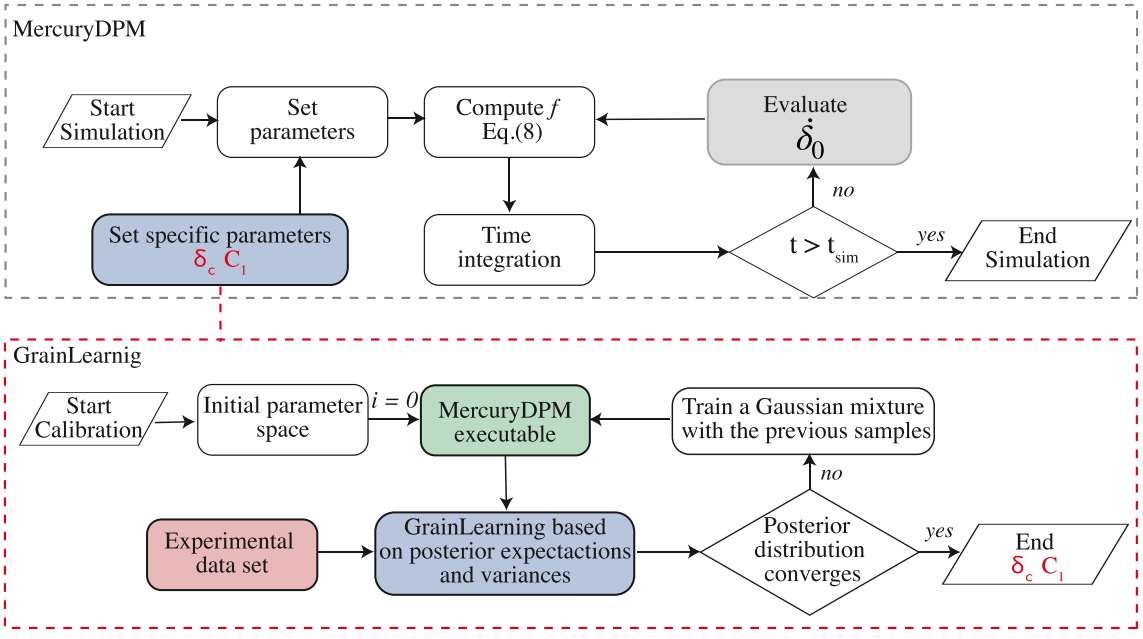

Fig. 7. Flowchart of the coupled implementation to find the parameters: δ_c, C_1, using MercuryDPM and `GrainLearning`. A MercuryDPM executable is called by `GrainLearning` at each iteration where the probabilities over δ_c and C_1 are updated with the neck growth data. The calibration is finished if the statistics converge in three consecutive iterations.

homogeneously. The oil reduces the adhesion between the particles and the glass plate. Then, the heating stage was cooled to room temperature, and a sample of individual virgin particles was selected manually and deposited onto the oil. Subsequently, the stage is re-heated to 195 °C at a rate of 150 °C/min. The coalescence of the particles was recorded using a digital microscope, using 20 frames per second and magnification between 200 and 500 times. A lower magnification was used to capture multiple particle pairs in one frame. After the complete merging of the particles, the stage was cooled back down to room temperature. The procedure was repeated twice to reproduce deteriorated states under the same conditions of sintering using virgin particles. The microscopy images of the sintering process in virgin and two-recycled states are depicted in Fig. 6.

The average particle radius is determined by fitting a circle adjacent to the contact point to the measured pixel area constituting each particle and measuring its radius at beginning time t_0. Virgin particles are not always spherical, so the measured radius is only approximated, whereas particles of first or second ageing cycles are resintered and thus nearly spherical. The software ImageJ, an open-source image processing program [24], was utilized to measure the pixel length. Furthermore, the software gives information about particle area, aspect ratio, circularity, Feret diameter, perimeter and roundness. It enables the approximation of the particle radius to be set into DEM simulations.

4.2. DEM calibration using `GrainLearning`

Microscopic material parameters relevant to sintering are extremely challenging to evaluate experimentally. Therefore, we treat the quantification of separation distance δ_c and fluidity C_1 as an inverse problem, that is to infer particle-scale parameters from experimental observations of the sintering kinetics. To this end, the iterative Bayesian filtering framework proposed by Cheng et al. [21] is coupled with MercuryDPM to calibrate the required sintering parameters. Fig. 7 presents the flowchart of this coupled implementation.

`GrainLearning` is a machine learning-based Bayesian calibration tool for estimating parameter uncertainties in discrete particle simulations. It uses the recursive Bayes' rule to quantify the evolution of the probability distribution of parameters over iterations. Samples are drawn either uniformly, assuming no prior knowledge, developing an improving proposal distribution that is learned over several iterations. After having enough statistics per iteration (effective sample size), we train and utilize nonparametric Gaussian mixture models as proposal distributions to resample the parameter space. The mixture model trained at the end of each iteration guides the resampling to be asymptotically close to optima, and thus greatly reduces the computational cost compared with conventional approaches.

For Bayesian calibration, the probability distribution of model states and parameters, conditioned on given reference data (termed "posterior distribution") can be approximated by sequential Monte Carlo methods. To efficiently sample parameter space, a multi-level (re)sampling algorithm is utilized. For the first iteration of Bayesian filtering, the parameter values are uniformly sampled from quasi-random numbers, which leads to conventional sequential quasi-Monte Carlo filtering. For the subsequent iterations, new parameter values are drawn from the posterior distribution from the previous iteration. Iterative Bayesian filtering allows us to sample near potential posterior modes in parameter space, with an increasing sample density over the iterations, until the ensemble predictions (e.g., expectations) of the model parameters converge.

5. Results and discussion

In the following section, the proposed approach is applied to analyse the visco-elastic sintering kinetics of polymer powders. Thus, the results using virgin and aged particles are described and compared to experimental data. Finally, the influence of particle shape and sintering stress during the neck growth are discussed.

5.1. Effect of viscoelasticity on polymer sintering

To simulate the visco-elastic sintering kinetics of polymer powders, a pair of 3D spheres of equal diameter is placed next to each other with negligible non-zero overlap between them. The particles are set just in contact at time t_0; the gravitational force is neglected. Fig. 8 illustrates the interpenetration between the two particles at four different time steps.

A small adhesive force $f^a = k_1\delta_a$ is applied to the particles to start the motion, where $\delta_a = 1.0 \times 10^{-3}$ m. Thereafter, the computation of the normal interaction updates the overlap δ. The geometrical relationship $a/R \approx \sqrt{\delta/R}$ can be obtained from the interaction, tracked at every time step in order to distinguish the sintering regime. All simulations use the material parameters listed in Table 1.

The magnitude of stiffness k_1 cannot be compared directly with the Young's modulus E of a material, since it is a contact property. However, an approximation micro to macro parameter exist to relate $k_1 \sim \beta E R$ [25], where $\beta = 1.0$ is chosen in our work. It leads to a contact duration (half-period) $t_c \approx 2.9 \times 10^{-7}$ μs, which is much smaller than the sintering time scale. Thus, the parameters in Table 1 only have a negligible effect on the sintering behaviour, which is determined by the evolution of δ_{ij}^0; they only affect how quickly oscillations due to the particle's inertia are damped. Young's modulus E, surface tension γ, Poisson's ratio η, and instantaneous compliance C_0 are set according to the type of materials analyzed in the present work. The magnitudes are listed in Table 2.

Two parameters remain to be calibrated in the contact model: δ_c and C_1. The parameters are calibrated via `GrainLearning` according to the sort of polymer and aged state. For this, the posterior probability distribution is estimated for all samples and materials with 50 model evaluations per iteration. The normalized covariance parameter at the first iteration is set to 0.7, resulting in an effective sample size larger than 20%. The goal is to have a sufficient number of effective statistical samples for estimating the proposal distribution to continue the iterations. Table 3 lists the upper and lower limits of δ_c and C_1, for which a Halton sequence is generated.

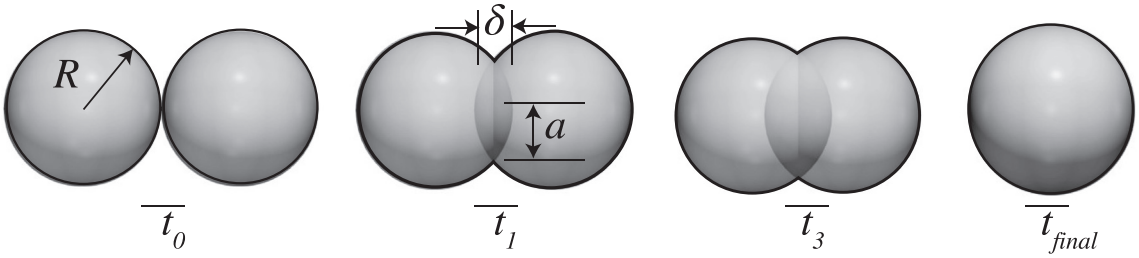

Fig. 8. Simulation of two spherical particles using MercuryDPM. The snapshots are taken from four different time steps where $a/R = 0.0$, $a/R = 0.2$, $a/R = 0.5$, $a/R = \sqrt[3]{2}$.

Table 1
System properties.

ρ [kg/m^3]	k_1 [N/m]	k_2 [N/m]	k_c [N/m]	e	φ
1000	$\beta E R$	2.0 k_1	1.0 k_1	0.1	$\sqrt[3]{4}$

The agreement of the posterior expectations before and after one iteration of Bayesian filtering is adopted as the convergence criterion. The posterior expectation of each micro-parameter converges after the third iteration. The illustration of the re-sampling process is presented in Fig. 9, which depicts the posterior modes localized progressively after each iteration for PA12, as an example. Note that if the initial guess for the model parameters is not able to capture at least one posterior distribution, the re-sampling scheme could explore outside the parameter ranges specified in Table 3, at the cost of more iterations and model evaluations.

5.1.1. Virgin powder

The first analysis corresponds to the sintering of polymers in a virgin state. The calibration of δ_c and C_1 is performed by `GrainLearning` using experimental data on PA12, PS [22], and PEEK [6]. Table 4 lists the results of the Bayesian calibration.

High precision is obtained, with only $1.0 \approx 3.0$ % range of error. Furthermore, the correlation of $\delta_c(R)$ is obtained as $\delta_c/R \approx 0.01$, as suggested by Lin et al. [8]. The visco-elastic sintering kinetic of PA12 particles is presented in Fig. 10.

The experimental results show the non-linear sintering path first, corresponding to the visco-elastic behaviour of the material. The transition between the second and third sintering mechanisms is at $t_{vis} = 0.5$ s, when $a/R \approx 0.22$. The maximum overlap ($a/R = 1.0$) is crossed at $t = 3.7$ s. This overlap means that particles have still a distinctive radius. After this point, particles merge to complete the sintering at $a/R = \sqrt[3]{2}$. It is reached at $t_{final} = 5.6$ s. To compare the precision of the simulation result, the original and modified Frenkel models are calibrated using the best approximation at the maximum overlap, using $\eta = 3355.0$ Pa s. However, Frenkel models anticipate neck growth during the early stage of the process. It leads to the over-prediction of the sintering time for short sintering since the driving force for coalescence is equivalent during the process.

The neck-growth estimation for PS is plotted in comparison with the experimental data in Fig. 11.

An important consequence in the sintering of polymer powders is that the process is faster for materials with low molecular weight [26]. This is the case for PS, in which the stress relaxation occurs within $t_{vis} = 0.01$ s. Thereafter, the visco-elastic mechanism dominates the process to complete the full consolidation at $t_{final} = 0.11$ s for $R = 30.0$ μm and $t_{final} = 0.27$ s for $R = 60.0$ μm. Thereby, the influence of particle radius is highly relevant in the process, as evidenced by the retardation for sintering. The maximum penetration depth was set to match the experimental merging radius at $a/R = 1.1$. This limitation was due to particles were not able to fully relax as spherical droplets experimentally [22]. It is demonstrated that PS powder can be well-described by the proposed three-stage sintering model. Furthermore, Frenkel's equations are calibrated based on the best approximation at the merged particle radius, using $\eta = 93.0$ Pa s. As the viscosity is increased, Frenkel's model may decrease the neck growth rate. However, this would retard the coalescence by leading to an inaccurate approximation.

Table 2
Material properties.

Material	E [Pa]	γ [N/m]	η	C_0 [Pa^{-1}]
PA12	1.94×10^9	40.0×10^{-3}	0.35	2.58×10^{-10}
PS	1.23×10^9	35.6×10^{-3}	0.34	4.08×10^{-10}
PEEK 450PF	3.60×10^9	35.0×10^{-3}	0.40	1.39×10^{-10}

Table 3
Upper and lower limits of the parameters to generate homogeneous quasi-random numbers for the first iteration.

Property	δ_c [μm]	C_1 [Pa^{-1} s^{-1}]
Θ_{min}	0.01	1.0×10^{-3}
Θ_{max}	9.0	1.0×10^{1}

The third analysis is conducted on PEEK 450PF and PEEK HP3, as reported by Berretta et al. [6]. Fig. 12 depicts the results.

The sintering of PEEK 450PF and PEK HP3 illustrates the implication of polymers with high viscosity. The relaxation for flowability is reached at $t_{vis} = 12.0$ s, at about 36% of the interpenetration on PEEK 450PF, and $t_{vis} = 9.0$ s, at about 34% of the interpenetration on PEK HP3. The highest slope was achieved by PEK HP3, followed by PEEK 450PF over the same time interval. It indicates that the second polymer is higher in molecular weight leading to less shrinkage. From the experimental results, it is observed the non-linear and visco-elastic kinetics of the material. This is remarkably predicted using the proposed contact model through the action of forces that involve two principal rheological characteristics, namely fluidity and elastic behaviours. These attributes determine the transport mechanism under the action of diffusive forces and stress, imposed either by thermal conditions or by mechanical action or by the combination of the two. It is relevant to mention that the particle radius used for the computations was set as the one measured at the beginning of the experiments, as reported by Berretta et al [6]. It may influence the prediction in the initial stage since the particles were in amorphous shapes. Frenkel's equations are calibrated based on the best approximation at the merged particle radius, using $\eta = 23000.0$ Pa s. It also indicates that the flowability is not good at high temperatures for this type of polymers.

5.1.2. Aged powder

To characterize polymer sintering under different aged conditions, we performed experiments based on a recycled scheme. The experimental data were collected in two different scenarios. First, the sintering process is repeated twice immediately after forming the consolidation from the virgin state; it was directly developed at the hot stage as presented in Fig. 6. Second, virgin PA12 powder was annealed inside an oven for 7 and 14 hours at a temperature of 160 °C (below the melting point of 180 °C). Then, the hot stage microscopy technique was employed to measure neck growth. Subsequently, `GrainLearning` is utilized to estimate δ_c and C_1 based on the observations. Table 5 lists the calibrated parameters to set within the contact model.

After every usage (sintering), a trend of around 50% reduction in C_1 is observed relative to the previous situation. This is reasonable since viscosity increases in aged states, which means a lower fluidity. Conversely, the separation distance δ_c remains roughly steady, increasing by 1%. Fig. 13 displays the results of the sintering process for the first aged state.

In aged states, polymer sintering is slower as evidenced in Fig. 13. The 100% of neck growth is achieved at $t = 7.7$ s. This is twice the time required using virgin powder (see Fig. 10). The transition time, at which the second and third sintering mechanisms change, is at $t_{vis} = 1.1$ s; δ_c/R continues roughly steady. The two procedures to recycle PA12 led to similar experimental results. It suggests that particle properties are in a similar deteriorated state if they suffer heating conditions or if they are reused immediately after the first sintering process. Fig. 14 presents the neck-growth kinetics of the second aged state.

After sintering virgin powder twice, the maximum overlap $a/R = 100\%$ is obtained at about $t = 13$ s, which takes almost three times longer than the time required using virgin powder. Frenkel's models start to agree well with the experimental data at longer times due to the

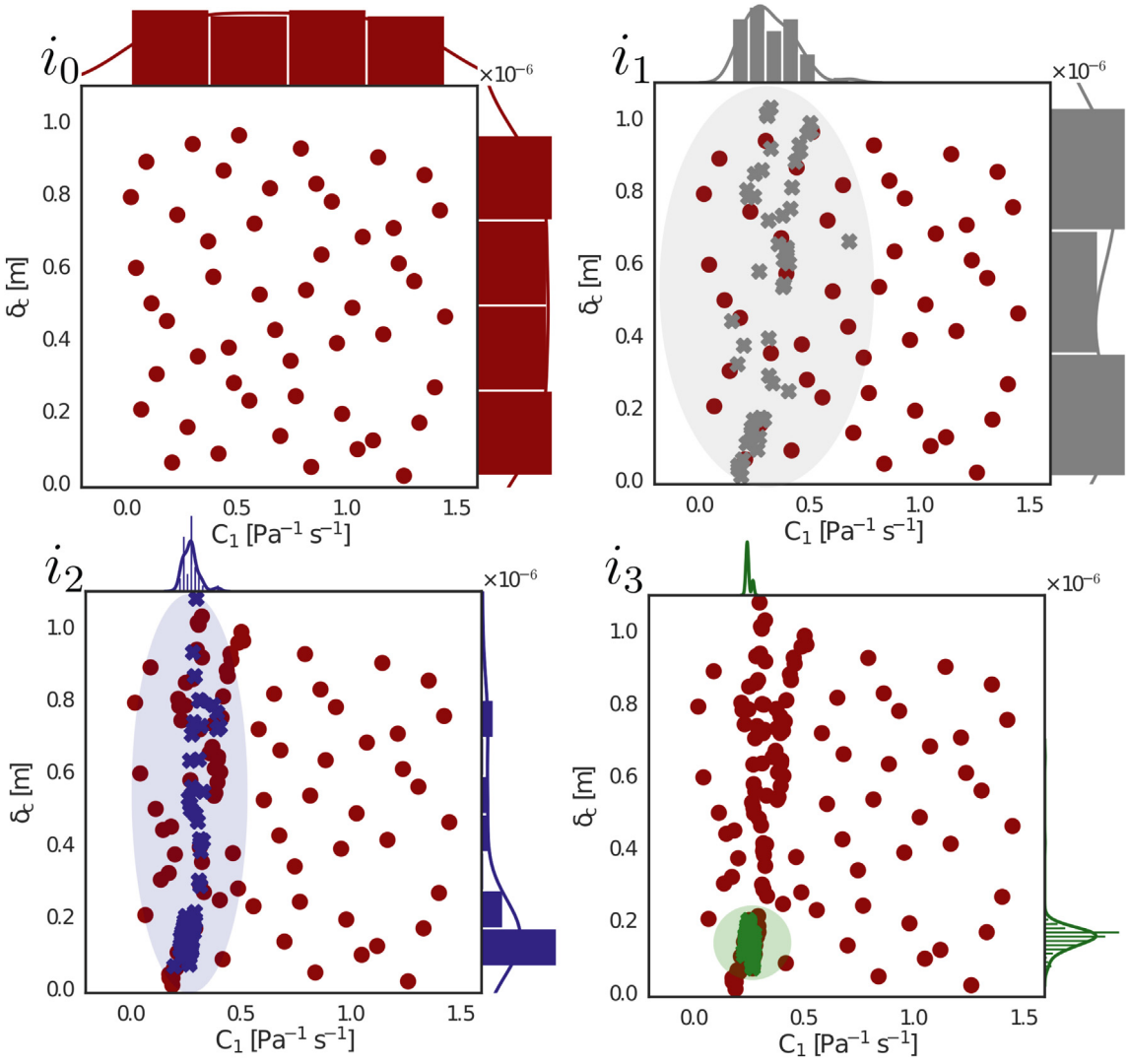

Fig. 9. Calibration of δ_c and C_1 for sintering simulations of PA12 with $R = 33.63$ μm. Bars denote the sampling distribution of the current iteration (which is based on the posterior distribution of the previous iteration, except for the first iteration). Coloured dots indicate the distributions, that are progressively placed near the posterior modes over the iterations as the localized bars show. (For interpretation of the references to color in this figure legend, the reader is referred to the web version of this article.)

increased viscosity of the material in this state. The transition time between the second and third sintering mechanisms is at $t_{vis} = 1.9$ s, which is almost three times longer than the relaxation time sintering virgin particles.

Finally, Fig. 15 presents the three case studies for visco-elastic sintering using PA12.

The degradation level has a great influence on the growth rate as evidenced in Fig. 15. This suggests that a lack of the supplied energy while sintering recycled powder can lead to slower neck formation, and therefore, poor cohesion. The DEM prediction indicates that the balance between the relaxation time and the material compliance has a significant contribution to the sintering of visco-elastic polymers. In

Table 4
Calibrated micro-mechanical properties (virgin particles).

Material	R [μm]	δ_c [μm]	C_1 [Pa^{-1} s^{-1}]
PA12	32.1	0.28 ± 3.0 %	2.42 ± 1.0 %
PS	30.0	0.15 ± 1.0 %	65.20 ± 1.0 %
PS	60.0	0.41 ± 1.0 %	27.20 ± 1.0 %
PEEK 450PF	25.0	0.45 ± 2.0 %	0.30 ± 1.0 %
PEK HP3	25.0	0.31 ± 2.0 %	0.35 ± 1.0 %

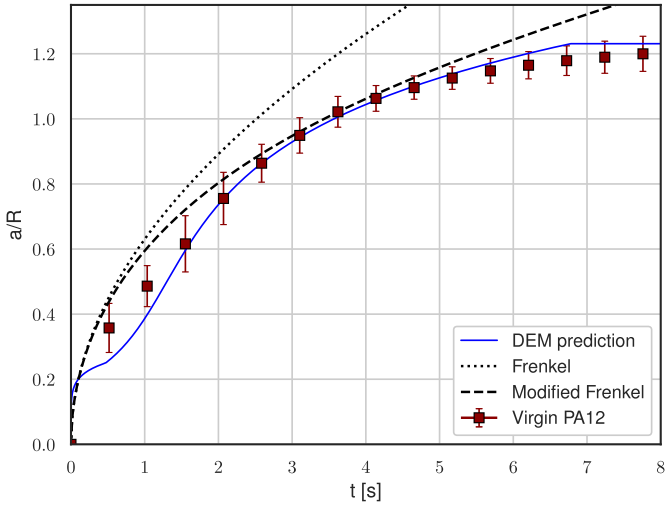

Fig. 10. Neck growth kinetics of virgin PA12. The solid line represents the calibrated DEM simulation with $R = 32.1$ μm. The dotted and dashed lines are obtained by fitting the original and modified Frenkel's models [27] to the experimental data with $\eta = 3355.0$ Pa s, respectively. Experimental observations are represented by the error bars.

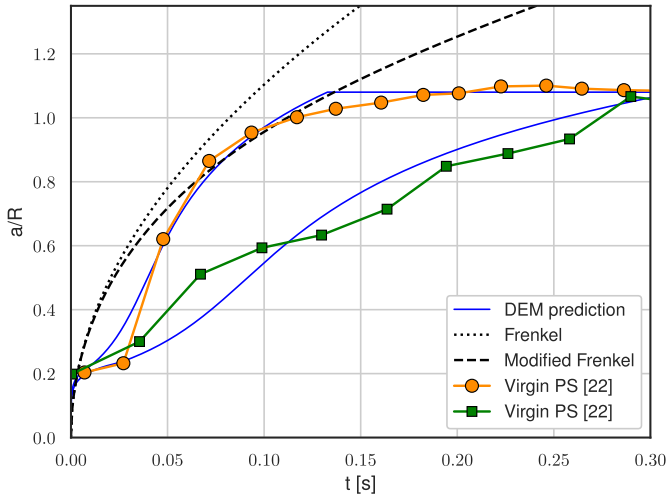

Fig. 11. Neck growth kinetics of virgin PS. The solid line represents the calibrated DEM simulation. The dotted and dashed lines are obtained by fitting the original and modified Frenkel's models [27] to the experimental data with $\eta = 93.0$ Pa s, respectively. Experimental observations are represented by dots for $R = 30.0$ μm, and squares for $R = 60.0$ μm, from [22].

fact, compliance is well known to be a sensitive function of molecular weight, and the visco-elastic kinetics must be analysed when modelling the sintering of polymers [12].

5.2. Influence of particle shape during sintering

Particles are modelled as perfect spheres in the sintering simulations. It leads to a homogeneous interaction at the particle-particle contact. However, polymers are not always available as spheres in a virgin state, see Fig. 6. To overcome this fact, the Feret diameter was measured on the experimental data, which is an option available in ImageJ software. This diameter was set to perform the simulations in MercuryDPM. The results showed good agreement independent of the low circularity at short times, which increases when polymer particles were subjected to temperatures close to the melting point. Furthermore, particles characteristics such as morphology, surface texture and porosity are not as

Table 5
Calibrated micro-mechanical properties.

Material	δ_c [μ m]	C_1 [Pa^{-1} s^{-1}]
Virgin PA12	0.28 ± 3.0 %	2.42 ± 1.0 %
1st Aged PA12	0.29 ± 2.0 %	1.01 ± 0.1 %
2nd Aged PA12	0.31 ± 2.0 %	0.49 ± 0.1 %

significant for the sintering rate at long times, and the shape evolution of the particle radius is independent of the flow history as suggested by Benedetii et al [10].

5.3. Sintering stress

When particles are sintering, outward-directed traction arises at the neck tip as a result of the balance of the compressive force acting on the contact (Fig. 16). The traction can be expressed by

$$\sigma_t = k_s \gamma, \tag{19}$$

where γ is surface tension, $k_s = 2R/a^2$ represents the relationship between curvature at the neck tip and contact radius a [11].

As the particles approach the common radius during sintering, the curvature at the neck increases significantly, which becomes very large just before reaching the merging radius. During this period, a debonding process may occur by external forces, leading to the formation of defects. To analyse the stress evolution during the growth of the contact radius, the tangential response during sintering of virgin and aged PA12 particles is plotted in Fig. 17.

The sintering stress increases with time in the evolution of the contact radius. In the initial stage, a sharp peak is evidenced as the result of stress relaxation. Thereafter, this point marks the transition to mass transport due to surface tension. The contact radius grows continuously until the maximum radius, which implies the maximum stress during the process. As far as the virgin particles are aged as the higher stress reached during the consolidation. It means more energy is required to consolidate aged particles as evidenced in the neck growth kinetics (Fig. 15). The evolution of the tangential stress during the sintering process may be influenced by temperature gradients. As a consequence, local stresses may appear. Nonetheless, our experiments and

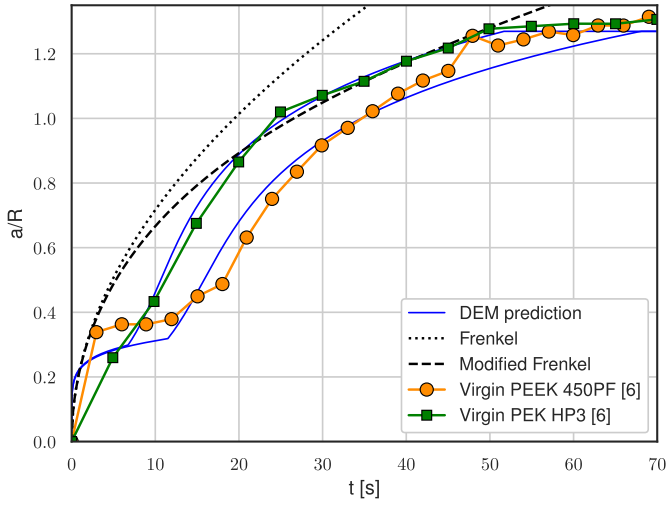

Fig. 12. Neck growth kinetics of virgin PEEK 450PF and PEK HP3. The solid line represents the calibrated DEM simulation with $R = 25.0$ μm. The dotted and dashed lines are obtained by fitting the original and modified Frenkel's models [27] to the experimental data with $\eta = 23000.0$ Pa s. Experimental observations are represented by dots for PEEK 450PF and squares for PEK HP3, from [6].

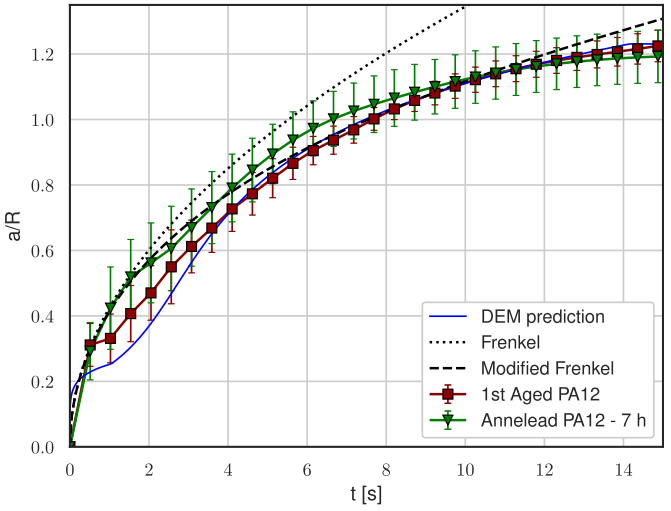

Fig. 13. Neck growth kinetics of aged PA12 with $R = 33.7$ μm. Squares represent the observations immediately after the first sintering. Triangles correspond to PA12 particles annealed inside an oven for 7 hours. The dotted and dashed lines are obtained by fitting original and modified Frenkel's models [27] to the experimental data with $\eta = 7550.0$ Pa s.

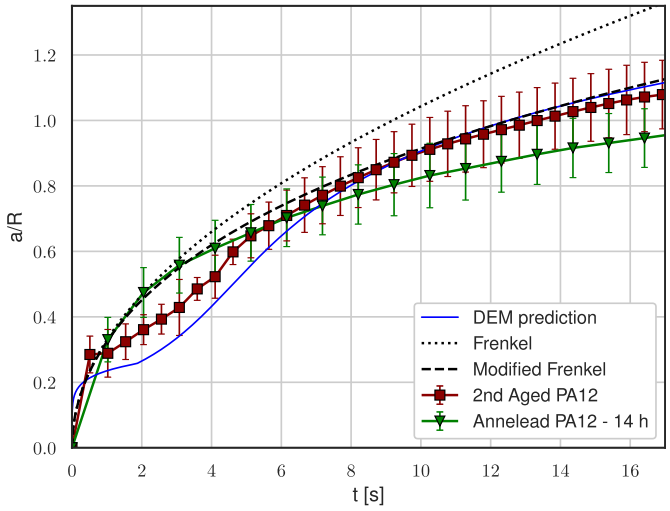

Fig. 14. Neck growth kinetics of second aged PA12 with $R = 33.63\ \mu$m. Squares represent the observations immediately after the previous sintering. Triangles correspond to PA12 particles annealed in an oven for 14 hours. The dotted and dashed lines are obtained by fitting original and modified Frenkel's models [27] to the experimental data, with $\eta = 12500.0$ Pa s.

simulations were conducted under a controlled temperature regime, which allowed us to predict the sintering rate for all experiments.

6. Conclusions

Our main result is that the sintering of visco-elastic powders is accurately and quantitatively predictable, at both short and long time scales. This is successfully achieved in our DEM framework by modelling the non-linear behaviour and including three different sintering mechanisms. The presented model requires only two sintering parameters to be calibrated in the simulations. This calibration was performed using `GrainLearning` package, where the probabilistic distributions of the parameters and their correlations were inferred precisely. Even though the model does not account for the anisotropy of visco-elastic materials, it allows analysing cases where particles are recycled in two scenarios: reused powder from a previous sintering process and powder annealed inside an oven for several hours. All predictions show a remarkable agreement with the experimental observations on PA12, PS, and PEEK particles. It demonstrates the impact of this approach on the prediction of sintering times.

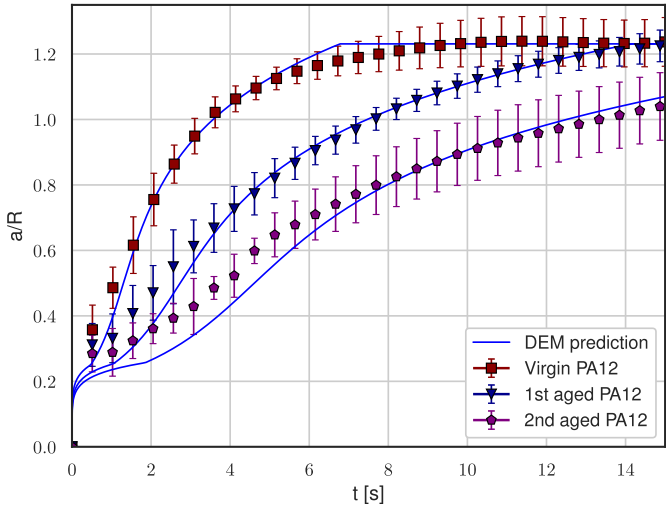

Fig. 15. Neck growth kinetics of PA12 in virgin and aged states. Experimental observations are represented by squares, triangles and pentagons for virgin, first aged and second aged, respectively. Solid lines describe the DEM prediction.

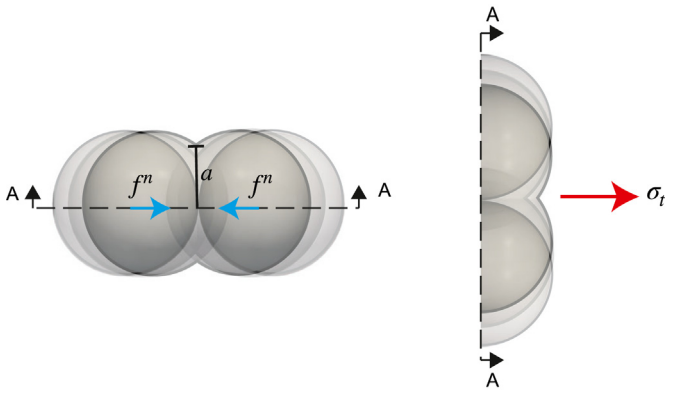

Fig. 16. Evolution of the contact radius a during the sintering process. f^n represents the normal force and σ_t the tangential sintering stress.

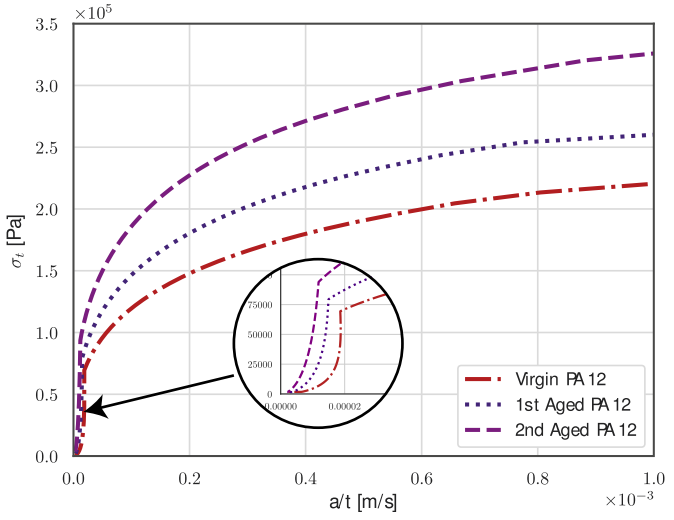

Fig. 17. Stress evolution at the neck tip vs. the rate of contact radius for PA12 in virgin and aged states.

7. Outlook

The proposed approach will be utilized in future DEM studies to analyse the strength evolution by particle cohesion, including different powder usage histories and temperature gradients. Thus, a better understanding of the grade of virgin and re-used particles can be assessed to avoid surface defects from the poor cohesion of sintered layers. In general, re-used powder requires a slower processing speed.

The present calculations refer to mono-disperse particles with spherical shapes. Future calculations will consider other possible particle distributions, and a multi-particle scheme to describe amorphous conditions. Furthermore, future studies on the sintering of aggregates will include the time-dependence of the radius based on the conservation of mass.

Data availability statement

The data presented are available in a publicly accessible repository of 4TU.ResearchData: https://figshare.com/s/8c8db15956482a17c2c3

Declaration of Competing Interest

The authors declare that they have no known competing financial interests or personal relationships that could have appeared to influence the work reported in this paper.

Acknowledgments

This work was financially supported by NWO-TTW grant No.16604 Virtual Prototyping of Particulate Processes (ViPr) - Design and Optimisation via Multiscale Modelling and Rapid Prototyping.

References

[1] G. Guan, M. Hirsch, Z.H. Lu, D.T. Childs, S.J. Matcher, R. Goodridge, K.M. Groom, A.T. Clare, Evaluation of selective laser sintering processes by optical coherence tomography, Mater. Des. 88 (2015) 837–846, https://doi.org/10.1016/j.matdes.2015.09.084.

[2] M. Markl, C. Körner, Powder layer deposition algorithm for additive manufacturing simulations, Powder Technol. 330 (2018) 125–136, https://doi.org/10.1016/j.powtec.2018.02.026 URL https://linkinghub.elsevier.com/retrieve/pii/S0032591018301475.

[3] J. Frenkel, Viscous flow of crystalline bodies under the action of surface tension, J. Phys. 9 (1945) 385.

[4] S. Haeri, L. Benedetti, O. Ghita, Effects of particle elongation on the binary coalescence dynamics of powder grains for Laser Sintering applications, Powder Technol. 363 (2020) 245–255, https://doi.org/10.1016/j.powtec.2019.12.025.

[5] R. Fuchs, T. Weinhart, M. Ye, S. Luding, H.J. Butt, M. Kappl, Initial stage sintering of polymer particles – experiments and modelling of size-, temperature- and time-dependent contacts, EPJ Web of Conferences, Vol. 140, EDP Sciences 2017, pp. 1–4, https://doi.org/10.1051/epjconf/201714013012.

[6] S. Berretta, Y. Wang, R. Davies, O.R. Ghita, Polymer viscosity, particle coalescence and mechanical performance in high-temperature laser sintering, J. Mater. Sci. 51 (10) (2016) 4778–4794, https://doi.org/10.1007/s10853-016-9761-6.

[7] M. Zhao, D. Drummer, K. Wudy, M. Drexler, Sintering study of polyamide 12 particles for selective laser melting, Int. J. Recent Contrib. Eng. Sci. IT (iJES) 3 (1) (2015) 28, https://doi.org/10.3991/ijes.v3i1.4290 URL https://online-journals.org/index.php/i-jes/article/view/4290.

[8] Y.Y. Lin, C.Y. Hui, A. Jagota, The role of viscoelastic adhesive contact in the sintering of polymeric particles, J. Colloid Interface Sci. 237 (2) (2001) 267–282, https://doi.org/10.1006/jcis.2001.7470 URL https://www.sciencedirect.com/science/article/pii/S0021979701974703.

[9] K. Johnson, K. Kendall, A. Roberts, Surface energy and the contact of elastic solids, Proc. R Soc. London. A Math. Phys. Sci. 324 (1558) (1971) 301–313, https://doi.org/10.1098/rspa.1971.0141 URL https://royalsocietypublishing.org/doi/10.1098/rspa.1971.0141.

[10] L. Benedetti, B. Brulé, N. Decraemer, K.E. Evans, O. Ghita, Evaluation of particle coalescence and its implications in laser sintering, Powder Technol. 342 (2019) 917–928, https://doi.org/10.1016/j.powtec.2018.10.053.

[11] K. Shinagawa, Simulation of grain growth and sintering process by combined phase-field/discrete-element method, Acta Mater. 66 (2014) 360–369, https://doi.org/10.1016/j.actamat.2013.11.023 URL https://linkinghub.elsevier.com/retrieve/pii/S1359645413008732.

[12] S. Mazur, D.J. Plazek, Viscoelastic effects in the coalescence of polymer particles, Prog. Org. Coat. 24 (1-4) (1994) 225–236, https://doi.org/10.1016/0033-0655(94)85016-X URL https://www.sciencedirect.com/science/article/pii/003306559485016X.

[13] C.T. Bellehumeur, M. Kontopoulou, J. Vlachopoulos, The role of viscoelasticity in polymer sintering, Rheol. Acta 37 (3) (1998) 270–278, https://doi.org/10.1007/s003970050114.

[14] S. Nosewicz, J. Rojek, K. Pietrzak, M. Chmielewski, Viscoelastic discrete element model of powder sintering, Powder Technol. 246 (2013) 157–168, https://doi.org/10.1016/j.powtec.2013.05.020 URL https://linkinghub.elsevier.com/retrieve/pii/S0032591013003689.

[15] M. Van den Eynde, L. Verbelen, P. Van Puyvelde, Assessing polymer powder flow for the application of laser sintering, Powder Technol. 286 (2015) 151–155, https://doi.org/10.1016/j.powtec.2015.08.004 URL https://www.sciencedirect.com/science/article/pii/S003259101530005X.

[16] K. Chockalingam, V.G. Kouznetsova, O. van der Sluis, M.G. Geers, 2D Phase field modeling of sintering of silver nanoparticles, Comput. Method. Appl. Mech. Eng. 312 (2016) 492–508, https://doi.org/10.1016/j.cma.2016.07.002.

[17] J. Laube, V. Baric, S. Salameh, L. Mädler, L. Colombi Ciacchi, A new contact model for the discrete element method simulation of TiO_2 nanoparticle films under mechanical load, Granular Matter. 20 (2) (2018) 28, https://doi.org/10.1007/s10035-018-0799-9 URL https://doi.org/10.1007/s10035-018-0799-9.

[18] F. Rizzi, M. Khalil, R.E. Jones, J.A. Templeton, J.T. Ostien, B.L. Boyce, Bayesian modeling of inconsistent plastic response due to material variability, Comput. Method. Appl. Mech. Eng. 353 (2019) 183–200, https://doi.org/10.1016/j.cma.2019.05.012.

[19] S. Luding, K. Manetsberger, J. Müllers, A discrete model for long time sintering, J. Mech. Phys. Solids 53 (2) (2005) 455–491, https://doi.org/10.1016/j.jmps.2004.07.001 URL https://www.elsevier.com/locate/jmps.

[20] T. Weinhart, L. Orefice, M. Post, M.P. van Schrojenstein Lantman, I.F. Denissen, D.R. Tunuguntla, J.M. Tsang, H. Cheng, M.Y. Shaheen, H. Shi, P. Rapino, E. Grannonio, N. Losacco, J. Barbosa, L. Jing, J.E. Alvarez Naranjo, S. Roy, W.K. den Otter, A.R. Thornton, Fast, flexible particle simulations - an introduction to MercuryDPM, Comput. Phys. Commun. 249 (2020) 107129, https://doi.org/10.1016/j.cpc.2019.107129.

[21] H. Cheng, T. Shuku, K. Thoeni, P. Tempone, S. Luding, V. Magnanimo, An iterative Bayesian filtering framework for fast and automated calibration of DEM models, Comput. Method. Appl. Mech. Eng. 350 (2019) 268–294, https://doi.org/10.1016/j.cma.2019.01.027 URL https://www.sciencedirect.com https://www.elsevier.com/locate/cma https://creativecommons.org/licenses/by/4.0/.

[22] P. Hejmady, L.C. Van Breemen, P.D. Anderson, R. Cardinaels, Laser sintering of polymer particle pairs studied by in situ visualization, Soft Matter. 15 (6) (2019) 1373–1387, https://doi.org/10.1039/c8sm02081g URL https://pubs.rsc.org/en/content/articlehtml/2019/sm/c8sm02081g https://pubs.rsc.org/en/content/articlelanding/2019/sm/c8sm02081g.

[23] S. Luding, Cohesive, frictional powders: contact models for tension, Granular Matter. 10 (4) (2008) 235–246, https://doi.org/10.1007/s10035-008-0099-x URL https://www2.msm.ctw.utwente.nl/sluding/PAPERS/GM_CHOPScontacts.pdf.

[24] C.A. Schneider, W.S. Rasband, K.W. Eliceiri, NIH Image to ImageJ: 25 Years of Image Analysis, 2012 julhttps://doi.org/10.1038/nmeth.2089 URL https://www.nature.com/articles/nmeth.2089.

[25] S. Nosewicz, J. Rojek, M. Chmielewski, K. Pietrzak, D. Lumelskyj, Application of the Hertz formulation in the discrete element model of pressure-assisted sintering, Granular Matter. 19 (1) (2017) 16, https://doi.org/10.1007/s10035-016-0699-9.

[26] S. Mazur, R. Beckerbauer, J. Buckholz, Particle size limits for sintering polymer colloids without viscous flow, Langmuir 13 (16) (1997) 4287–4294, https://doi.org/10.1021/la970104w URL https://pubs.acs.org/doi/abs/10.1021/la970104w.

[27] O. Pokluda, C.T. Bellehumeur, J. Vlachopoulos, Modification of frenkel's model for sintering, AIChE J. 43 (12) (1997) 3253–3256, https://doi.org/10.1002/aic.690431213 URL https://aiche.onlinelibrary.wiley.com/doi/full/10.1002/aic.690431213 https://aiche.onlinelibrary.wiley.com/doi/abs/10.1002/aic.690431213 https://aiche.onlinelibrary.wiley.com/doi/10.1002/aic.690431213.